Article

Magnetic, Electronic, and Optical Studies of Gd-Doped WO$_3$: A First Principle Study

Ali Bahadur [1,*,†], Tehseen Ali Anjum [2,†], Mah Roosh [3,†], Shahid Iqbal [3,*], Hamad Alrbyawi [4], Muhammad Abdul Qayyum [5], Zaheer Ahmad [6], Murefah Mana Al-Anazy [7], Eslam B. Elkaeed [8], Rami Adel Pashameah [9], Eman Alzahrani [10] and Abd-ElAziem Farouk [11]

1 Department of Chemistry, College of Science and Technology, Wenzhou-Kean University, Wenzhou 325060, China
2 Nanomagnetism Laboratory, Department of Physics, COMSATS University Islamabad, Islamabad 45550, Pakistan
3 Department of Chemistry, School of Natural Sciences (SNS), National University of Sciences and Technology (NUST), H-12, Islamabad 46000, Pakistan
4 Pharmaceutics and Pharmaceutical Technology Department, College of Pharmacy, Taibah University, Medina 42353, Saudi Arabia
5 Department of Chemistry, Division of Science & Technology, University of Education, Lahore 54770, Pakistan
6 Department of Chemistry, University of Wah, Quaid Avenue, Wah Cantt 47040, Pakistan
7 Department of Chemistry, College of Science, Princess Nourah bint Abdulrahman University, P.O. Box 84428, Riyadh 11671, Saudi Arabia
8 Department of Pharmaceutical Sciences, College of Pharmacy, AlMaarefa University, Riyadh 13713, Saudi Arabia
9 Department of Chemistry, Faculty of Applied Science, Umm Al-Qura University, Makkah 24230, Saudi Arabia
10 Department of Chemistry, College of Science, Taif University, P.O. Box 11099, Taif 21944, Saudi Arabia
11 Department of Biotechnology College of Science, Taif University, P.O. Box 11099, Taif 21944, Saudi Arabia
* Correspondence: abahadur@wku.edu.cn (A.B.); shahidgcs10@yahoo.com (S.I.)
† These authors contributed equally to this work.

Abstract: Tungsten trioxide (WO$_3$) is mainly studied as an electrochromic material and received attention due to N-type oxide-based semiconductors. The magnetic, structural, and optical behavior of pristine WO$_3$ and gadolinium (Gd)-doped WO$_3$ are being investigated using density functional theory. For exchange-correlation potential energy, generalized gradient approximation (GGA+U) is used in our calculations, where U is the Hubbard potential. The estimated bandgap of pure WO$_3$ is 2.5 eV. After the doping of Gd, some states cross the Fermi level, and WO$_3$ acts as a degenerate semiconductor with a 2 eV bandgap. Spin-polarized calculations show that the system is antiferromagnetic in its ground state. The WO$_3$ material is a semiconductor, as there is a bandgap of 2.5 eV between the valence and conduction bands. The Gd-doped WO$_3$'s band structure shows few states across the Fermi level, which means that the material is metal or semimetal. After the doping of Gd, WO$_3$ becomes the degenerate semiconductor with a bandgap of 2 eV. The energy difference between ferromagnetic (FM) and antiferromagnetic (AFM) configurations is negative, so the Gd-doped WO$_3$ system is AFM. The pure WO$_3$ is nonmagnetic, where the magnetic moment in the system after doping Gd is 9.5599575 μB.

Keywords: Gd-doped; WO$_3$; first-principle study; antiferromagnetic; bandgap tuning

1. Introduction

The exclusive ability to induce bistable electrical and optical characteristics in WO$_3$ with different excitation sources makes it very promising among significant technological devices [1–4]. The element that has three oxygen atoms is called the perovskite-like structure. WO$_3$ has useful applications in optical and spintronic devices [5–7]. It is used for the construction of semiconductor-based gas sensors (SGS) and electrochromic devices

such as high-temperature superconductors (HTS), smart windows, solar cells, and water-splitting applications. The addition of electrons/holes could alter the characteristics of WO_3. Additionally, the possibility of ion intercalation/deintercalation arises in several possible applications in rechargeable batteries. Especially, the photocatalytic activities and SGS properties of WO_3 can be modified by doping transitional elements such as Au, Pd, and Pt. Rare earth and transition metal-doped WO_3 systems show interesting magnetic properties that usually do not exist in undoped WO_3 [8–10]. In this study, the magnetic, electronic, and optical properties of Gd-doped WO_3 are investigated by using first principle calculations. Here is a brief description of previous works related to WO_3. The monoclinic WO_3 is the most communal and stable phase of WO_3 with space group P21/n. The unit cell comprises 8W atoms and 24O atoms and holds 8O atoms at the corner in somewhat distorted cubic arrangements [11,12].

For the RT monoclinic, the direct bandgap calculated by using generalized gradient approximation (GGA) was increased initially as the volume decreased but, after that, decreases again with a further decrease in the volume. The cubic structure space groups Pm-3m contain basic structural characteristics but ignore distortion. The indirect bandgap of the cubic is smaller than the bandgap of the RT monoclinic. Low-temperature (LT) monoclinic structures with space groups Pc are other distorted forms of WO_3. The unit cell of LT monoclinic contains 4W atoms and 12O atoms. The bandgap at a low-temperature (LT) monoclinic is, to some extent, greater than the RT monoclinic. This shows a direct bandgap with the conduction band minimum (CBM) and valence band maximum (VBM). The triclinic structures have space groups P-1 and contain 8W and 24O atoms. The bandgap of the triclinic is a direct bandgap. The orthorhombic structure of WO_3 with a space group of P_{mnb} also has distorted oxygen-octahedrons [13,14]. The unit cell consists of 8W and 24O atoms. The bandgap is larger than the cubic and tetragonal ones but smaller than the monoclinic and triclinic structures [15].

The current studies showed that the assimilation of Gd^{3+} ion and other rare earth element ions in large bandgap semiconductor fallouts in boosting ferromagnetic properties inspired scientists on the way to rare earth elemental ion doping in various oxide nano-materials for spintronics applications. Especially, the Gd^{3+} ion has more potential due to its optical and magnetic properties [16]. It was reported that WO_3 is translucent in visible light, but strong absorption arises in near-infrared regions because of the phonon–electron interaction [17]. The reflectance and transmittance of WO_3 material were noted in the range 400–2600 nm at P_{tot} = 10 and 30 mTorr. The dielectric function of the monoclinic and triclinic are comparable and cannot be separated by their dispersion relation. The optical gap is 2.5 to 2.6 eV, which is less than that of TiO_2, and absorbs adequate visible radiations to produce a photocurrent. According to UV–Vis diffuse reflectance, WO_3, bare light absorbs at a wavelength of less than 460 nm, which gives an energy bandgap of 2.6 eV. In Gd-WO_3, 4% absorption significantly transfers towards a longer wavelength from 460 to 470 nm along a bandgap of 2.64 eV. This perception is associated with the reality that hybridization occurs between O $2p$ and Gd $4f$/$5d$ orbitals alternatively and is incorporated into the WO_3 lattice [18].

Bullet, Stashans, and Lunnel observed the effect of the interaction of alkali ions on the cubic, room temperature monoclinic and Perovskite structure of WO_3 [19]. The WO_3 electronic structure and sub-stoichiometry are informally connected to the properties of the structure. O $2p$ orbitals are present in the valence band, and W $5d$ orbitals are present in the conduction band. The phase transition outcome in the W $5d$ states causes changes in the energy gap. They concluded that the upward shift in the W $5d$ states changes the ideal cubic structure to a monoclinic structure and increases E_g from 1.5 to 2.45 eV [20].

The bandgap value of WO_3 changes experimentally from 2.6 to 3.2 eV. This is due to the changes in the structure of WO_3 [21]. The significance of the surface area and the interphase boundary is of great importance [22–27]. The insufficient oxygen WO_{3-x} is connected to the effect on the electrical properties and color, and the color changes from greenish to yellowish in WO_3. In nanostructure WO_3 films processed by reactive sputtering,

E_g has linked to the O_2 sputtering pressure and the vacancy of the O concentration. For the various phases of WO_3 alternations in E_g with *d* orbital occupancy, the points of the VBM and CBM have been recognized. The calculation of cubic WO_3 with the density functional theory (DFT) computations underreported at about 0.6 eV correlated with the value of the experimental value of 2.6 eV. In the dispersion of the band close to the region Nd–gap, the γ-WO_3, δ-WO_3, β-WO_3, and ε-WO_3 phases are observed, which are less by the initial calculations, which is due to the small difference in the lattice constant and short difference in the bond angle [17,28].

Even though only insufficient theoretical/experimental research has been done to discover the electronic/magnetic properties of RT monoclinic WO_3, it is needed to explore the bandgap, energy band, and electron/hole reshuffle. Momentum density studies of WO_3 have not been conducted up to now. WO_3 exists in more than one crystalline form. The most common structure of WO_3 is cubic, as for ReO_3 [29–31]. The crystal structure of WO_3 depends on the temperature when the temperature rises above 770 °C, its crystal shape is tetragonal; between 330 °C and 740 °C, it is orthorhombic; between 17 °C and 33 °C, it is monoclinic; and between −50 °C and 17 °C, it is triclinic [32–34]. Momentum density studies of WO_3 have been not conducted to date. Even though only insufficient theoretical/experimental research has been done to discover the electronic/magnetic properties of RT monoclinic WO_3, it is needed to explore bandgap, energy band, and electron/hole reshuffle. In the present work, the electronic, magnetic, and optical properties of Gd-doped WO_3 are investigated by using first principle calculations. GGA+U approximation is applied to the orthorhombic structure to calculate the density of the states and optical and magnetic properties of WO_3.

2. Simulation and Calculations

The full potential linear augmented plane wave (FPLAPW) method with the WEIN2k code is used to calculate the optical, electrical, and magnetic properties of pure WO_3 and Gd-doped WO_3 [35]. The lattice parameters of pure WO_3 are: a = 7.303, b = 7.5389, and c = 7.6896 A, and those of Gd-doped WO_3 are a = 7.303, b = 7.5389, and c = 15.3724 A. The space group number of WO_3 is 14P21/n, and K-mesh points 21 × 21 × 10 were used. The electronic charge density "ECD" expanded up to G_{max} = 12. In the interstitial region "IR", the plane wave "PW" cut-off value is K_{max} = 6.5/RMT. The size of the supercell is 21 × 21 × 10, and it contains 16 atoms. The optical and magnetic properties of the orthorhombic-like structure WO_3 are calculated using GGA+U approximation. The element that has three oxygen atoms is called the perovskite-like structure. The orthorhombic structure is shown in Figure 1.
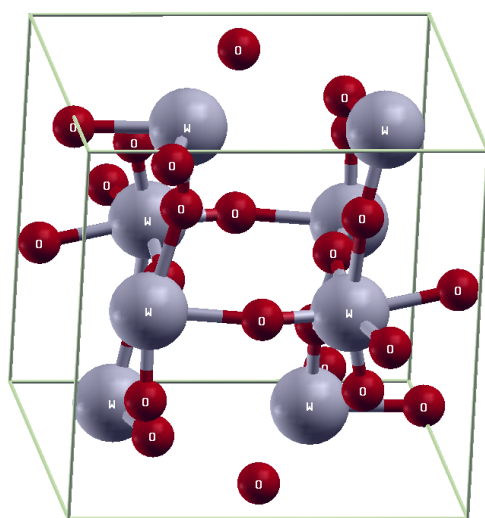

Figure 1. Orthorhombic structure of WO_3.

3. Results and Discussion

Figure 2 represents the total density of the states of WO$_3$ before and after the doping of Gd, a rare earth metal. There is no absolute energy taken along the x-axis but the Fermi energy. Fermi energy is an approach in quantum mechanics that usually mentions the highest filled states of single particles in a quantum system of noninteracting fermions at absolute zero temperature. In Figure 2a, no states reside in the Fermi level for pure WO$_3$. In Figure 2b, after the doping of Gd, some states reside in the Fermi level when the system is ferromagnetic (FM), which means that all the unpaired electrons have the same spin directions. In Figure 2c, some states reside in the Fermi level after the doping of Gd when the system has antiferromagnetic materials (AFM), which means that all the unpaired electrons have a spin moment in the antiparallel direction.
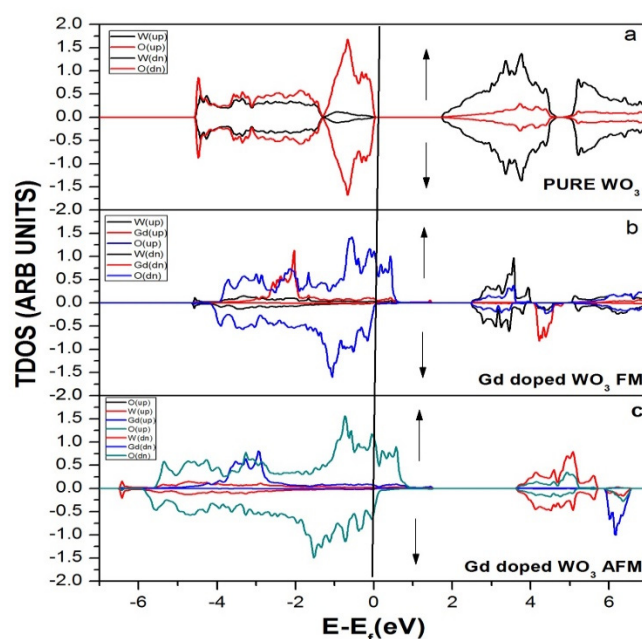

Figure 2. Density of the states (DOS) of (**a**) pure WO$_3$, (**b**) Gd-doped WO$_3$ FM, and (**c**) Gd-doped WO$_3$ AFM by using GGA+U approximation.

Figure 3 represents the partial density of the states. GGA+U approximation is used for the calculation of Gd-doped WO$_3$. For calculating the partial density of the states, W has the states of *s*, *p*, *d*, and *f*, and O has *s* and *p*, while Gd has the *s*, *p*, *d*, and *f* states. Many clear states reside in the bandgap after the doping of the Gd rare earth metal. In the case of pure WO$_3$, no states exist in the bandgap, as shown in Figure 3a, but after the doping of Gd, some states reside that cross the Fermi level, as shown in Figure 3b,c. Both calculations are done by using the GGA+U approximations. According to Figure 4, the material is a semiconductor, as there is a bandgap of 2.5 eV between the valence band and conduction band [36]. Figure 4 represents the band structure of pure WO$_3$, which shows the direct bandgap. Figure 4a is the spin-up band, and Figure 4b is the spin-down direction.
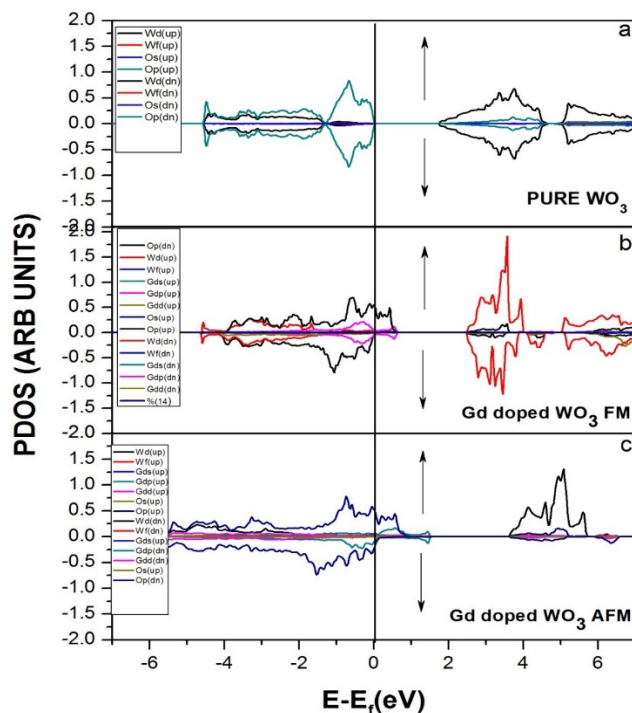
Figure 3. Projected DOS (PDOS) of (**a**) pure WO_3, (**b**) Gd-doped WO_3 FM, and (**c**) Gd-doped WO_3 AFM by using GGA+U approximation.

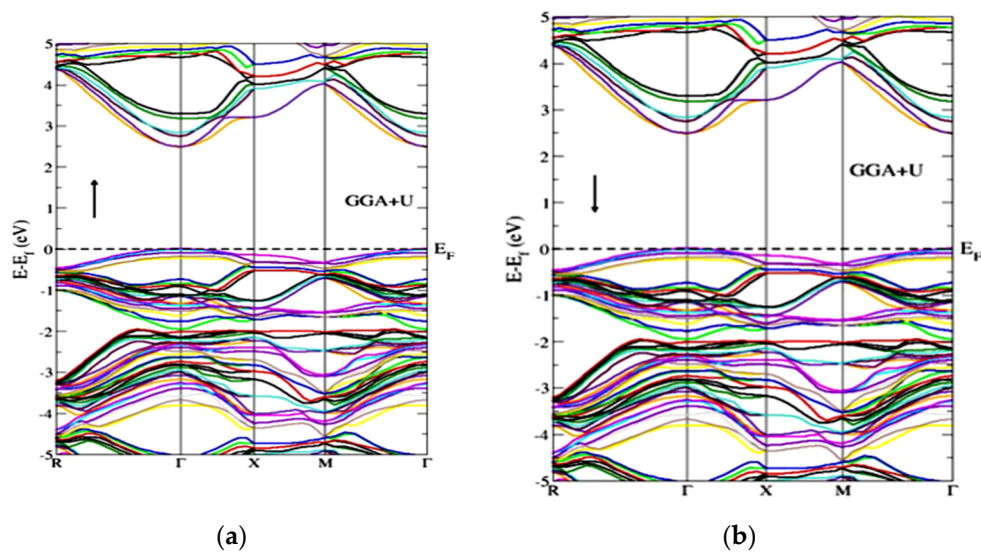|	
(**a**)	(**b**)

Figure 4. Band structure of pure WO_3 for the (**a**) spin-up and (**b**) spin-down directions by using GGA+U approximation.

Figure 5 represents the band structure of Gd-doped WO_3 for spin-up and spin-down in the FM configuration. It shows that few states cross the Fermi level, which means that the material is metal or semimetal. Figure 5 represents the gap inside the conduction band. From Figure 5, after the doping of Gd, WO_3 becomes the degenerate semiconductor. The degenerate semiconductor shows a metallic character after high doping.
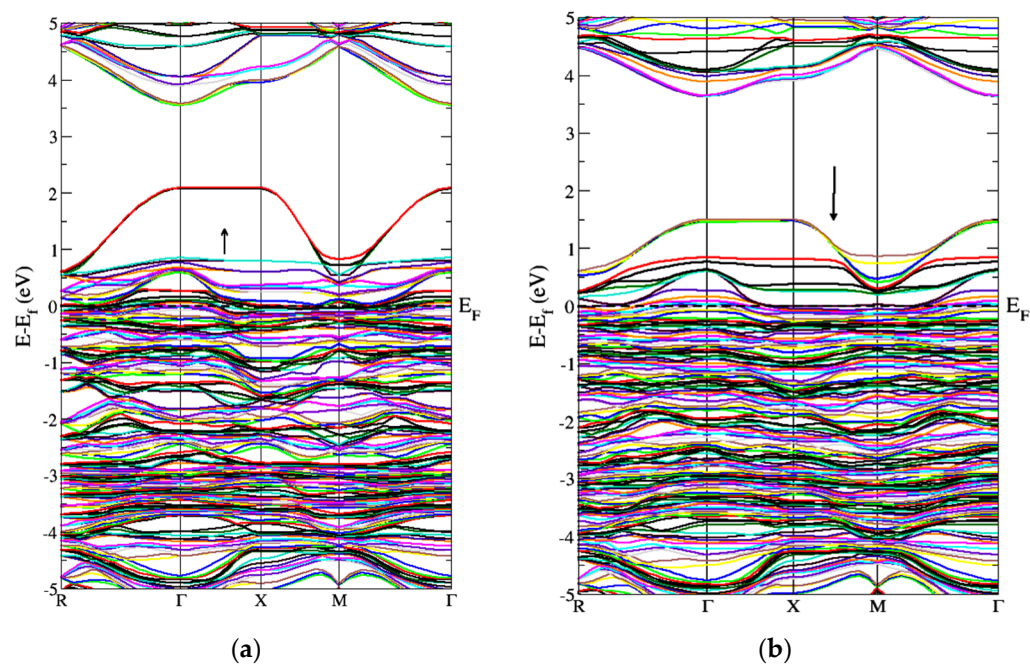
Figure 5. Band structure of Gd-doped WO$_3$ for FM calculations (**a**) spin-up and (**b**) spin-down.

Figure 6 represents the band structure of the Gd-doped WO$_3$ by AFM calculations. Figure 6 is for the spin-up and spin-down directions after WO$_3$ doping by Gd. As the states lie inside the Fermi level, it shows a metallic character after the doping of the Gd metal. Figure 6 also shows that, after the doping of Gd, the WO$_3$ semiconductor becomes a degenerate semiconductor. As the energy difference between the FM and AFM configurations is negative, the Gd-doped WO$_3$ system is AFM, according to the calculations, and the energy is calculated in millielectron volts. The pure WO$_3$ is nonmagnetic, where the magnetic moment in the system after doping Gd is 9.5599575 μB (Table 1).
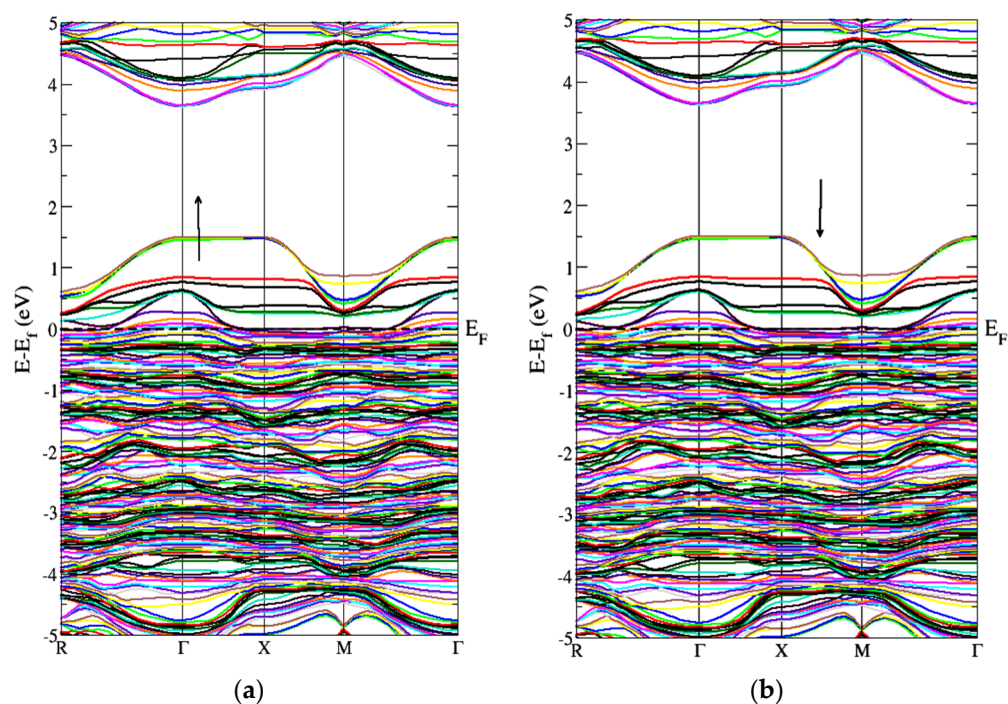

Figure 6. Band structure of Gd-doped WO$_3$ for AFM calculations (**a**) spin-up and (**b**) spin-down.

Table 1. Magnetic properties of Gd-doped WO_3.

Compound	Supercell Size	$\triangle E = E_{AFM} - E_{FM}$ (meV)	Coupling	Spin Magnetic Moment in Supercell (μB)
Gd: WO_3	$21 \times 21 \times 10$	-1.05815002	AFM	9.5599575

Figure 7 represents the absorption coefficient of WO_3 and Gd-doped WO_3. Figure 7a indicates that, in pure WO_3, the absorption increases gradually at energy 2 eV, which is the threshold energy for absorption and is equivalent to the bandgap energy. However, after the doping of the Gd rare earth element, there is a clear difference in the absorption of WO_3, as the curve starts rising from 0 eV, as shown in Figure 7b,c, which means that the material becomes metallic or semi-metallic.
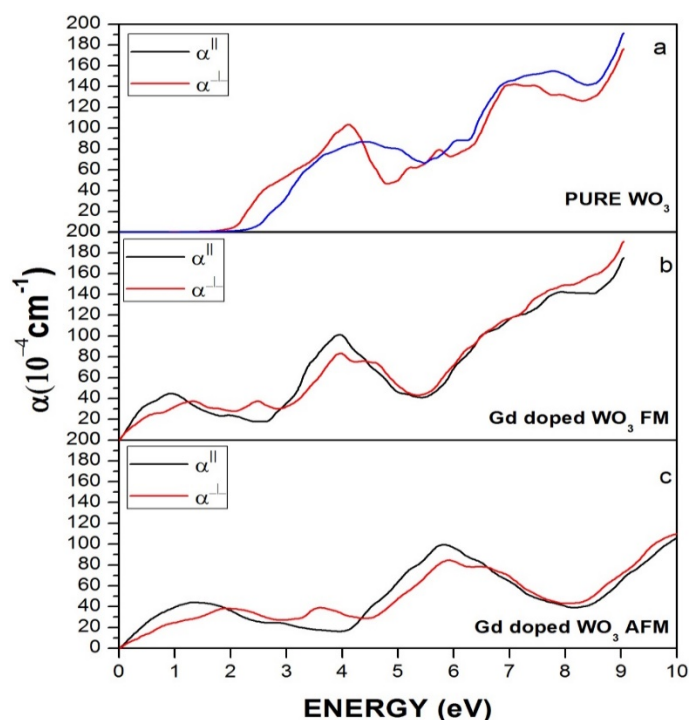

Figure 7. Absorption of (**a**) pure WO_3, (**b**) Gd-doped WO_3 for FM, and (**c**) Gd-doped WO_3 for the AFM configuration.

Figure 8 represents the real part of the dielectric function for pure and doped WO_3 in FM and AFM configurations. In Figure 8a, the perpendicular component lies in the negative region in the energy range 6–7 eV, which shows that the material behaves reflective in this energy range and is transparent in the rest of the energy region. However, after the doping of Gd, as shown in Figure 7b,c, the states mostly lie above zero points, and very few states are below zero points. A clear reduction in the states below zero points happened. Figure 8b is FM Gd-doped WO_3, and Figure 8c is Gd-doped WO_3 in the AFM configuration. Gd causes a reduction of the states below zero points, which shows that the material became nonreflective.
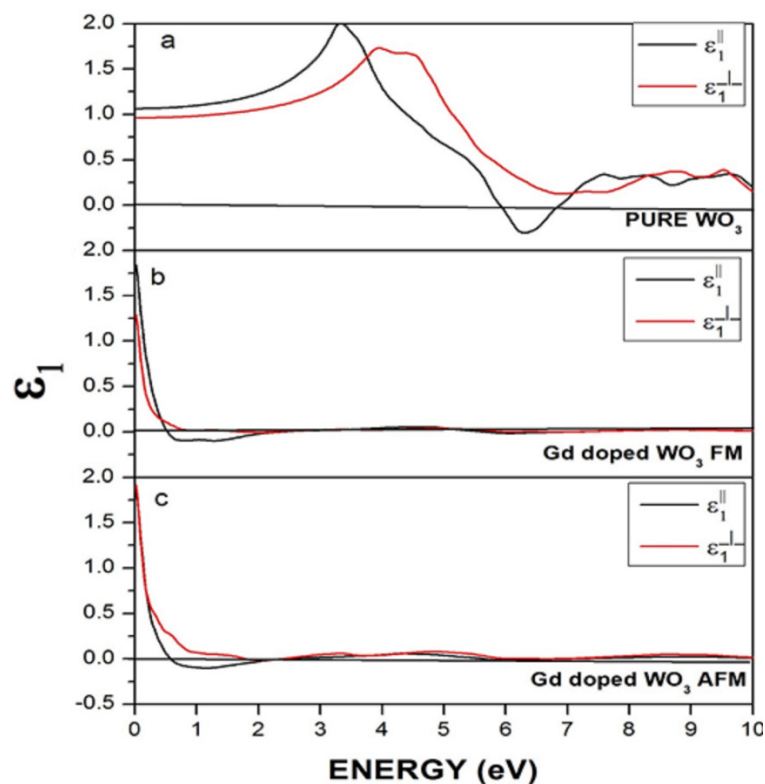
Figure 8. Real dielectric function of (**a**) pure WO$_3$, (**b**) Gd-doped WO$_3$ for FM, and (**c**) Gd-doped WO$_3$ for the AFM configuration.

A material's complex dielectric function consists of two parts: real $\varepsilon_1(\omega)$ and imaginary $\varepsilon_2(\omega)$ (Figure 9). The absorption of photons is represented by the imaginary part of the dielectric function and electronic transition from valence towards the conduction band. The equation for $\varepsilon_2(\omega)$ can be written as:

$$\varepsilon_2(\omega) = \frac{4\pi^2 e^2}{m^2 \omega^2} \sigma_{ij} \int \langle i|M|j \rangle^2 f_i (1 - f_i) \delta(E_j - E_i - \omega) d^3k \qquad (1)$$

where M represents the dipole matrix, the free electron is represented by m, for the initial and final states, the i and j symbols are used, the ith state Fermi distribution is represented by f_i, and E_i and E_j are the energy of the free electrons in the initial and final states.
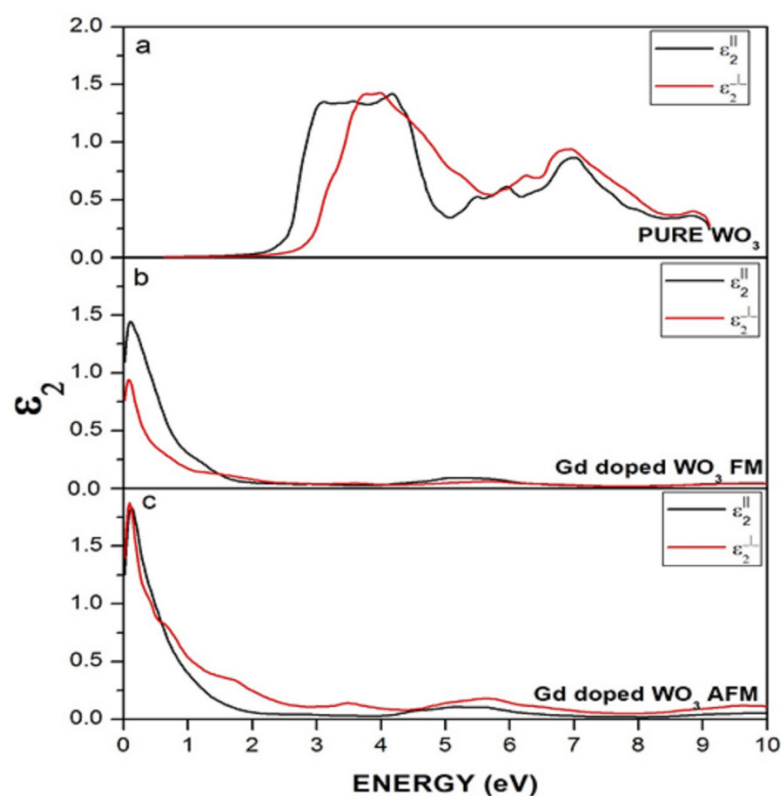
Figure 9. Imaginary dielectric function of (**a**) WO$_3$, (**b**) Gd-doped WO$_3$ for FM, and (**c**) Gd-doped WO$_3$ for the AFM configuration.

4. Conclusions

In the present work, the electronic, magnetic, and optical properties of pure WO$_3$ and Gd-doped WO$_3$ were calculated by using the GGA+U approximation for exchange–correlation energy. The energy difference between the FM and AFM configurations showed that the Gd-doped WO$_3$ system is AFM. Pure WO$_3$ is a nonmagnetic semiconductor with a bandgap of 2.5 eV. The system becomes a degenerate semiconductor after the doping of the rare earth element Gd in WO$_3$. In the real dielectric function of WO$_3$, the perpendicular component lies in the negative region in the energy range 6–7 eV, which shows that the material behaves as reflective in this energy range and is transparent in the rest of the energy region. The spin-polarized calculations showed that the system is antiferromagnetic in its grounded state. The WO$_3$ material is a semiconductor, as there is a bandgap of 2.5 eV between the VB and CB. Pure WO$_3$ is nonmagnetic, where the magnetic moment in the system after doping Gd is 9.5599575 µB.

Conflicts of Interest: The authors declare no conflict of interest.

References

1. Dören, R.; Leibauer, B.; Lange, M.A.; Schechtel, E.; Prädel, L.; Panthöfer, M.; Mondeshki, M.; Tremel, W. Gram-scale selective synthesis of WO_3-x nanorods and $(NH_4)xWO_3$ ammonium tungsten bronzes with tunable plasmonic properties. *Nanoscale* **2021**, *13*, 8146–8162. [CrossRef]
2. Prasad, U.; Young, J.L.; Johnson, J.C.; McGott, D.L.; Gu, H.; Garfunkeld, E.; Kannan, A.M. Enhancing interfacial charge transfer in a $WO_3/BiVO_4$ photoanode heterojunction through gallium and tungsten co-doping and a sulfur modified Bi_2O_3 interfacial layer. *J. Mater. Chem. A* **2021**, *9*, 16137–16149. [CrossRef]
3. Li, J.; Guo, C.; Li, L.; Gu, Y.; Kim, B.-H.; Huang, J. Synthesis of vertical WO_3 nanoarrays with different morphologies using the same protocol for enhanced photocatalytic and photoelectrocatalytic performances. *RSC Adv.* **2021**, *11*, 23700–23706. [CrossRef]
4. Deng, C.-B.; Zhang, M.; Lan, T.; Zhou, M.-J.; Wen, Y.; Zhong, J.; Sun, X.-Y. Spectroscopic investigation on Eu_{3+}-doped TeO_2-Lu_2O_3-WO_3 optical glasses. *J. Non-Cryst. Solids* **2021**, *554*, 120565. [CrossRef]
5. Shen, L.; Zheng, J.; Xu, C. Enhanced electrochromic switches and tunable green fluorescence based on terbium ion doped WO_3 films. *Nanoscale* **2019**, *11*, 23049–23057. [CrossRef] [PubMed]
6. Tahir, M.B.; Sagir, M. Carbon nanodots and rare metals (RM = La, Gd, Er) doped tungsten oxide nanostructures for photocatalytic dyes degradation and hydrogen production. *Sep. Purif. Technol.* **2019**, *209*, 94–102. [CrossRef]
7. Palanisamy, G.; Bhuvaneswari, K.; Bharathi, G.; Pazhanivel, T.; Grace, A.N.; Pasha, S.K. Construction of magnetically recoverable $ZnS–WO_3–CoFe_2O_4$ nanohybrid enriched photocatalyst for the degradation of MB dye under visible light irradiation. *Chemosphere* **2021**, *273*, 129687. [CrossRef]
8. Li, Y.; Liu, Z.; Li, J.; Ruan, M.; Guo, Z. An effective strategy of constructing a multi-junction structure by integrating a heterojunction and a homojunction to promote the charge separation and transfer efficiency of WO_3. *J. Mater. Chem. A* **2020**, *8*, 6256–6267. [CrossRef]
9. Gopakumar, G.; Nair, S.V.; Shanmugam, M. Assessing the role of plasma-engineered acceptor-like intra- and inter-grain boundaries of heterogeneous $WS_2–WO_3$ nanosheets for photocurrent characteristics. *Nanoscale Adv.* **2020**, *2*, 2276–2283. [CrossRef]
10. Gong, H.; Hao, X.; Jin, Z.; Ma, Q. WP modified S-scheme $Zn_{0.5}Cd_{0.5}S/WO3$ for efficient photocatalytic hydrogen production. *New J. Chem.* **2019**, *43*, 19159–19171.
11. Çoban, Ö.; Gür, E.; Tüzemen, S. Platinum activated WO_3 optical hydrogen sensors. *Mater. Today Proc.* **2021**, *46*, 6913–6915. [CrossRef]
12. Zhang, Z.; Zhao, C.; Lin, S.; Li, H.; Feng, Y.; Gao, X. Oxygen vacancy modified Bi_2MoO_6/WO_3 electrode with enhanced photoelectrocatalytic degradation activity toward RhB. *Fuel* **2021**, *285*, 119171. [CrossRef]
13. Manikandan, V.S.; Harish, S.; Archana, J.; Navaneethan, M. Fabrication of novel hybrid Z-Scheme $WO_3@g-C_3N_4@MWCNT$ nanostructure for photocatalytic degradation of tetracycline and the evaluation of antimicrobial activity. *Chemosphere* **2022**, *287*, 132050. [CrossRef]
14. Muller, O.; Gibot, P. Optical limiting properties of templated Cr_2O_3 and WO_3 nanoparticles. *Opt. Mater.* **2019**, *95*, 109220. [CrossRef]
15. Huda, M.N.; Yan, Y.; Moon, C.-Y.; Wei, S.-H.; Al-Jassim, M.M. Density-functional theory study of the effects of atomic impurity on the band edges of monoclinic WO_3. *Phys. Rev. B* **2008**, *77*, 195102. [CrossRef]
16. Vijayaprasath, G.; Murugan, R.; Hayakawa, Y.; Ravi, G. Optical and magnetic studies on Gd doped ZnO nanoparticles synthesized by co-precipitation method. *J. Lumin.* **2016**, *17*, 375–383. [CrossRef]
17. Deb, S.K. Opportunities and challenges in science and technology of WO_3 for electrochromic and related applications. *Sol. Energy Mater. Sol. Cells* **2008**, *92*, 245–258. [CrossRef]
18. Guo, R.; Fang, L.; Dong, W.; Zheng, F.; Shen, M. Enhanced photocatalytic activity and ferromagnetism in Gd doped $BiFeO_3$ nanoparticles. *J. Phys. Chem. C* **2010**, *114*, 21390–21396. [CrossRef]
19. Granqvist, C.G. Electrochromic tungsten oxide films: Review of progress 1993–1998. *Sol. Energy Mater. Sol. Cells* **2000**, *60*, 201–262. [CrossRef]
20. Zhang, N.; Chen, D.; Niu, F.; Wang, S.; Qin, L.; Huang, Y. Enhanced visible light photocatalytic activity of Gd-doped $BiFeO_3$ nanoparticles and mechanism insight. *Sci. Rep.* **2016**, *6*, 26467. [CrossRef]
21. Yao, Y.; Liu, W.; Chan, Y.; Leung, C.; Mak, C.; Ploss, B. Studies of rare-earth-doped $BiFeO_3$ ceramics. *Int. J. Appl. Ceram. Technol.* **2011**, *8*, 1246–1253. [CrossRef]
22. Iqbal, S. Spatial Charge Separation and Transfer in L-Cysteine Capped NiCoP/CdS Nano-Heterojunction Activated with Intimate Covalent Bonding for High-Quantum-Yield Photocatalytic Hydrogen Evolution. *Appl. Catal. B Environ.* **2020**, *274*, 119097. [CrossRef]
23. Iqbal, S.; Bahadur, A.; Anwer, S.; Ali, S.; Saeed, A.; Irfan, R.M.; Li, H.; Javed, M.; Raheel, M.; Shoaib, M. Shape and phase-controlled synthesis of specially designed 2D morphologies of l-cysteine surface capped covellite (CuS) and chalcocite (Cu2S) with excellent photocatalytic properties in the visible spectrum. *Appl. Surf. Sci.* **2020**, *526*, 146691. [CrossRef]
24. Iqbal, S.; Bahadur, A.; Anwer, S.; Shoaib, M.; Liu, G.; Li, H.; Raheel, M.; Javed, M.; Khalid, B. Designing novel morphologies of l-cysteine surface capped 2D covellite (CuS) nanoplates to study the effect of CuS morphologies on dye degradation rate under visible light. *Cryst. Eng. Comm.* **2020**, *22*, 4162–4173. [CrossRef]

25. Iqbal, S.; Bahadur, A.; Ali, S.; Ahmad, Z.; Javed, M.; Irfan, R.M.; Ahmad, N.; Qamar, M.A.; Liu, G.; Akbar, M.B. Critical role of the heterojunction interface of silver decorated ZnO nanocomposite with sulfurized graphitic carbon nitride heterostructure materials for photocatalytic applications. *J. Alloys Compd.* **2021**, *858*, 158338. [CrossRef]

26. Irfan, R.M.; Tahir, M.H.; Khan, S.A.; Shaheen, M.A.; Ahmed, G.; Iqbal, S. Enhanced photocatalytic H_2 production under visible light on composite photocatalyst (CdS/NiSe nanorods) synthesized in aqueous solution. *J. Colloid Interface Sci.* **2019**, *557*, 1–9. [CrossRef]

27. Hussain, W.; Malik, H.; Bahadur, A.; Hussain, R.A.; Shoaib, M.; Iqbal, S.; Green, I.R.; Badshah, A.; Li, H. Synthesis and Characterization of CdS Photocatalyst with Different Morphologies: Visible Light Activated Dyes Degradation Study. *Kinet. Catal.* **2018**, *59*, 710–719. [CrossRef]

28. Pradhan, S.; Das, J.; Rout, P.; Das, S.; Mishra, D.; Sahu, D.; Srinivasu, V.; Nayak, B.; Verma, S.; Roul, B. Defect driven multiferroicity in Gd doped $BiFeO_3$ at room temperature. *J. Magn. Magn. Mater.* **2010**, *322*, 3614–3622. [CrossRef]

29. Biltz, W.; Lehrer, G.A.; Meisel, K. Zeitschrift für anorganische und allgemeine Chemie. *Rheniumtrioxyd II Mitt.* **1932**, *207*, 113–120.

30. Ablat, A.; Wu, R.; Mamat, M.; Li, J.; Muhemmed, E.; Si, C.; Wu, R.; Wang, J.-O.; Qian, H.; Ibrahim, K. Structural analysis and magnetic properties of Gd doped $BiFeO_3$ ceramics. *Ceram. Int.* **2014**, *40*, 14083–14089. [CrossRef]

31. Kumar, K.S.; Ramu, S.; Sudharani, A.; Ramanadha, M.; Murali, G.; Vijayalakshmi, R. Enhanced magnetic and dielectric properties of Gd doped $BiFeO_3$: Er nanoparticles synthesized by sol-gel technique. *Phys. E Low-Dimens. Syst. Nanostructures* **2020**, *115*, 113689. [CrossRef]

32. Salje, E.K.; Rehmann, S.; Pobell, F.; Morris, D.; Knight, K.S.; Herrmannsdörfer, T.; Dove, M.T. Crystal structure and paramagnetic behaviour of. *J. Phys. Condens. Matter* **1997**, *9*, 6563. [CrossRef]

33. Kehl, W.; Hay, R.G.; Wahl, D. The structure of tetragonal tungsten trioxide. *J. Appl. Phys.* **1952**, *23*, 212–215. [CrossRef]

34. Tanisaki, S. Crystal structure of monoclinic tungsten trioxide at room temperature. *J. Phys. Soc. Jpn.* **1960**, *15*, 573–581. [CrossRef]

35. Blaha, P.; Schwarz, K.; Madsen, G.K.H.; Kvasnicka, D. WIEN2k: An augmented plane wave+ local orbitals program for calculating crystal properties. *Mater. Trans.* **2001**, *45*, 1991–1993.

36. Bak, T.; Nowotny, J.; Rekas, M.; Sorrell, C.C. Photo-electrochemical hydrogen generation from water using solar energy. Materials-related aspects. *Int. J. Hydrogen Energy* **2002**, *27*, 991–1022. [CrossRef]